

Emergence of a spin microemulsion in spin-orbit coupled Bose-Einstein condensates

Ethan C. McGarrigle¹, Kris T. Delaney², Leon Balents³
and Glenn H. Fredrickson^{1,2,4*}

¹Department of Chemical Engineering, University of California,
Santa Barbara, 93106, California, USA.

²Materials Research Laboratory, University of California, Santa
Barbara, 93106, California, USA.

³Kavli Institute for Theoretical Physics, University of California,
Santa Barbara, 93106, California, USA.

^{4*}Department of Materials, University of California, Santa
Barbara, 93106, California, USA.

*Corresponding author(s). E-mail(s): ghf@ucsb.edu;
Contributing authors: emcgarrigle@ucsb.edu;
kdelaney@mrl.ucsb.edu; balents@ucsb.edu;

Abstract

Recent experiments have shown how the interplay between Bose statistics and spin-orbit coupling (SOC) can lead to superfluid liquid crystalline (stripe) analogues in cold atomic gases. For isotropic SOC in two spatial dimensions, a Rashba dispersion is encountered where a continuous ring of single-particle states constitutes a massive ground-state degeneracy. Here, we perform approximation-free field-theoretic simulations of ensembles of interacting Rashba bosons and find a spin microemulsion phase with bicontinuous, antiferromagnetic domains. The microemulsion emerges at elevated temperatures as the low-temperature stripe phase undergoes a Kosterlitz–Thouless-like transition and loses superfluidity. Momentum distribution calculations highlight a thermally broadened occupation of the Rashba circle of low-energy states with macroscopic and isotropic occupation around the ring. We provide a finite-temperature phase diagram that positions the emulsion as an intermediate, structured isotropic phase with residual quantum character before transitioning at higher temperature into a structureless normal fluid.

Keywords: Microemulsion, Spin-orbit Coupling, Bose-Einstein Condensates, Stripe Phase

Microemulsion phases are found throughout nature and in synthetic soft matter systems [1–3], most prominently in oil-water-surfactant mixtures [4–6]. Two immiscible species form enriched domains while often a third minority component stabilizes their interfaces, playing the role of a surfactant or amphiphile. Another example is ternary polymer blends, where two incompatible homopolymers can form a bicontinuous microemulsion in the presence of a high-molecular-weight diblock copolymer [7, 8]. Beyond the classical soft matter context are 2D electronic systems [9–11], such as metal-oxide-semiconductor field-effect transistors, where microemulsion-like phases are proposed as intermediate phases between Wigner crystals and Fermi liquids [12, 13]. Here we detail the first appearance of a microemulsion in simulated 2D ensembles of ultracold bosons, where the interplay of Rashba SOC, Bose statistics, and thermal fluctuations produce an antiferromagnetic microemulsion structure. Enabling this work are newly developed algorithms for finite-temperature numerical simulation of bosonic quantum field theories that are robust against the sign problem, enjoy near linear scaling with system size, and incorporate full thermal and quantum fluctuations [14, 15].

In contrast to electrons in traditional condensed matter systems, neutral cold atoms lack an inherent SOC. Nonetheless, recent experiments [16–19] have engineered a relativistic spin-momentum coupling in cold atom systems via Raman laser setups. In the case of ^{87}Rb condensates, experiments isolate two hyperfine levels in the total angular momentum $F = 1$ manifold to create a “pseudospin-1/2” system, which are then coupled by two-photon Raman transitions [20]. Many cold atom experiments access a 1D SOC with double-well minima in the single-particle dispersion. There, Bose condensation occurs into one or both minima at non-zero momentum, leading to a pseudospin polarized “plane wave” phase or a standing-wave “stripe” phase, respectively. The stripe phase is a superfluid analogue of a smectic liquid crystal and was experimentally realized recently, first by Li and colleagues in ^{23}Na condensates [21] and later in ^{87}Rb condensates [22].

Isotropic “Rashba” SOC links the atom’s spin state to both momentum components \hat{p}_x, \hat{p}_y equally, analogous to 2D Rashba electronic systems [23–25] where a continuous circle of degenerate minima appear within a band. Recent experiments have engineered a Rashba-like, 2D SOC using several Raman beams [26], but did not achieve the circular degeneracy found with true Rashba SOC. Thus far, experimental realizations of isotropic Rashba SOC in cold atoms have gone unreported, yet have garnered interest evidenced by several experimental proposals [27] and theoretical studies of semi-classical, $T = 0$, or mean-field behavior [28–32], none of which consider the possibility of a spin microemulsion phase. Even more exotic behavior has been speculated: that

true Rashba bosons could exhibit fractional Hall-like states [26] or undergo a statistical transmutation into composite fermions [33].

Here we begin with a second-quantized model for interacting, pseudospin-1/2 Rashba bosons and study their finite-temperature behavior using a new field-theoretic simulation technique. Our investigations reveal a new microemulsion phase with bicontinuous, antiferromagnetic pseudospin domains reflecting an isotropic occupation of the Rashba dispersion. We perform simulations at several SOC strengths and temperatures to compute a phase diagram and confirm the microemulsion's existence between a low-temperature superfluid spin-stripe phase and high-temperature paramagnetic, normal fluid.

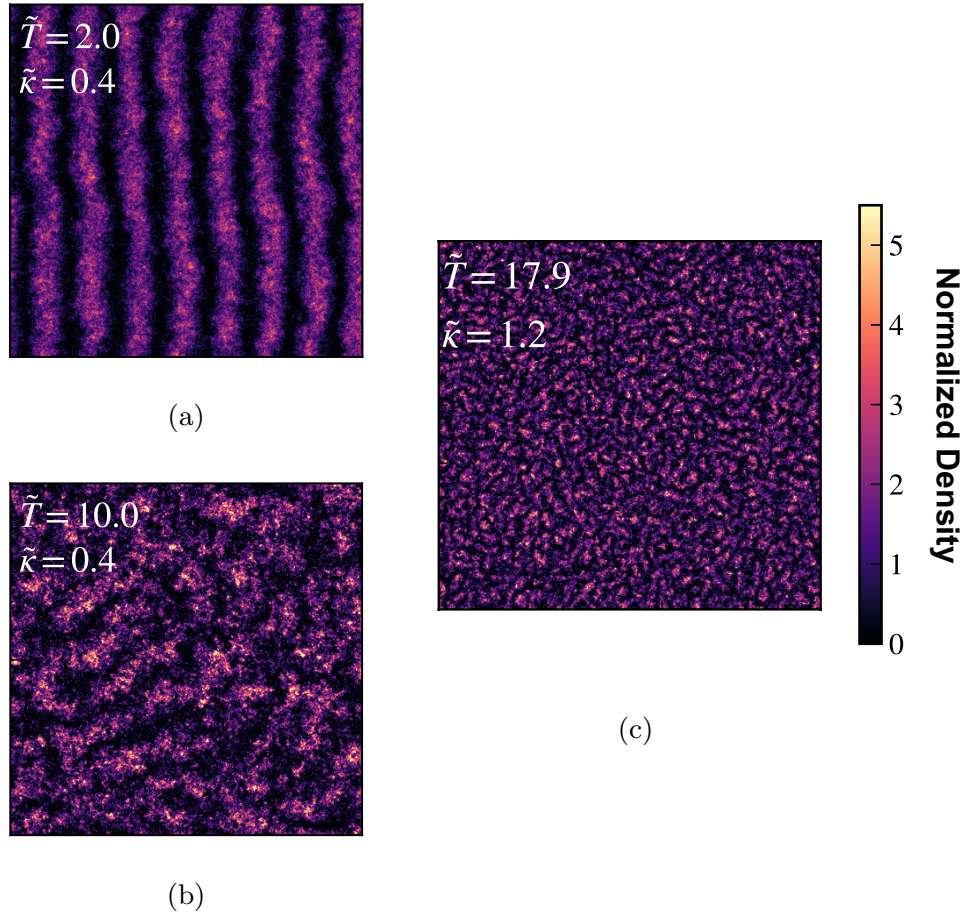


Fig. 1: Emergence of a microemulsion. Density profiles $\rho_{\uparrow}(\mathbf{r})$ of pseudospin bosons in the $|\uparrow\rangle$ basis state at interaction conditions $\tilde{g} = 0.05$, and $\eta_g = 1.1$. The left column depicts a phase transition between the **a.** superfluid stripe phase at $\tilde{\kappa} = 0.4$, $\tilde{T} = 2$ and **b.** microemulsion phase at $\tilde{\kappa} = 0.4$, $\tilde{T} = 10$. **c.** Emulsion phase with $\langle N \rangle \sim 4.8 \times 10^5$ particles in a larger field of view, $\tilde{\kappa} = 1.2$, $\tilde{T} = 17.9$. Profiles are snapshots normalized by the spatially averaged density.

We incorporate SOC into a model of interacting pseudospin-1/2 bosons via a uniform and time-independent non-Abelian gauge potential $\mathcal{A} = \hbar\kappa(\underline{\sigma}^x, \eta_\kappa \underline{\sigma}^y)$ [34], where $\underline{\sigma}^\nu$ are the spin-1/2 Pauli-matrices in the ν direction, κ is the SOC strength, and η_κ quantifies the anisotropy of the SOC. \mathcal{A} imbues the model with a sign problem and produces isotropic SOC when $\eta_\kappa = 1$, the case considered exclusively for this work. Assemblies of interacting pseudospin-1/2 bosons in 2D are well described by the second-quantized Hamiltonian:

$$\begin{aligned} \hat{H} = & \sum_{\alpha,\gamma} \int d^2r \, \hat{\psi}_\alpha^\dagger(\mathbf{r}) \left(\frac{1}{2m} [\hat{\mathbf{p}} \underline{I} - \mathcal{A}]^2 - \mu \underline{I} \right)_{\alpha\gamma} \hat{\psi}_\gamma(\mathbf{r}) \\ & + \frac{1}{2} \sum_{\alpha,\gamma} \int d^2r \, \hat{\psi}_\alpha^\dagger(\mathbf{r}) \hat{\psi}_\gamma^\dagger(\mathbf{r}) (g_0 \underline{I} + g_1 \underline{\sigma}^x)_{\alpha\gamma} \hat{\psi}_\alpha(\mathbf{r}) \hat{\psi}_\gamma(\mathbf{r}) \end{aligned} \quad (1)$$

where $\hat{\psi}_\alpha(\mathbf{r})$ are second-quantized field operators of pseudospin- α obeying Bose commutation relations [35], $\hat{\mathbf{p}} = -i\hbar\nabla$ is the canonical momentum operator, \underline{I} is the 2x2 identity matrix, μ is chemical potential, and m is the atomic mass shared by both pseudospin species. We assume contact pairwise interactions where the repulsive coupling constants g_0 and g_1 are parameterized by s-wave scattering lengths $a_{s,0}$ and $a_{s,1}$ for like and unlike pseudospin scattering events, respectively, and correspond to a symmetric matrix of coupling constants.

To simplify the analysis, we define a natural length scale $\ell = \sqrt{\frac{\hbar^2}{2m\mu_{\text{eff}}}}$ and energy scale μ_{eff} , where μ_{eff} is an effective chemical potential that incorporates the SOC recoil energy $\mu_{\text{eff}} \equiv \mu - \hbar^2\kappa^2/m$. After rescaling all field operators, spatial derivatives, and integrals using ℓ and μ_{eff} , we identify four dimensionless quantities that govern the model's universal behavior: a repulsion scale $\tilde{g} \equiv 2mg_0/\hbar^2$, a SOC strength $\tilde{\kappa} \equiv \kappa\ell$, a temperature $\tilde{T} \equiv k_B T/\mu_{\text{eff}}$, and a miscibility parameter $\eta_g \equiv g_1/g_0$. For this study, we confine our simulations to slightly immiscible conditions $\eta_g = 1.1 > 1$, which promote a stripe ground state at low temperatures.

To probe the equilibrium thermodynamics of the aforementioned model at finite temperature, we use Feynman's imaginary time path integral approach to convert the many-boson problem into a coherent state quantum field theory in the grand canonical ensemble [36]. In this formulation, the degrees of freedom are a complex conjugate pair of bosonic coherent state fields $(\phi_\alpha(\mathbf{r}, \tau), \phi_\alpha^*(\mathbf{r}, \tau))$ for each pseudospin species obeying periodic boundary conditions in imaginary time τ . The corresponding grand partition function is

$$\mathcal{Z} = \int \mathcal{D}(\phi, \phi^*) e^{-S[\phi, \phi^*]} \quad (2)$$

where $\mathcal{D}(\phi, \phi^*)$ is shorthand for functional integrals over the real and imaginary parts of the field components at each space-imaginary time point; ϕ and ϕ^* are additionally 2 component vectors in the pseudospin species. A

configuration's statistical weight is described by e^{-S} , where $S[\phi, \phi^*]$ is a complex-valued action functional (see Methods) that presents a numerically foreboding sign problem.

In our field-theoretic simulation method, we discretize the coherent state fields in the three space-imaginary time dimensions and numerically sample the field elements via a complex Langevin algorithm (see Methods). Our pseudospectral implementation assumes periodic boundary conditions in all dimensions. This procedure overcomes the statistical weight's highly oscillatory nature and provides bias-free thermodynamic properties at finite temperature [37, 38]. The computational burden of this “field-theoretic simulation” method enjoys near linear scaling with system size at fixed spatial resolution and, remarkably, is independent of the number of bosons. Observables of interest such as the pressure and internal energy are obtained by averaging field operators (functionals of the coherent state fields) over fictitious complex-Langevin time trajectories. Instantaneous values of field operators are complex along a trajectory, but the time average of a physical operator has vanishing imaginary part. [15]

To identify the presence of a stripe, microemulsion, or homogeneous phase, we equilibrated the system and calculated snapshots of the resulting structure's real-space density profile as well as thermal averages (via fictitious Langevin time averages) of the momentum state distribution in \mathbf{k} -space, where \mathbf{k} is the wavevector labelling momentum states. Thermal averages are computed by averaging decorrelated samples throughout a simulation. Above the stripe melting temperature, simulation results were insensitive to the initial field configuration; however, for the low temperature stripe regime, we initialized finite-temperature complex Langevin simulations with defect-free vertical stripe structures with \hat{x} density modulations, generated using the Langevin algorithm without noise (mean-field theory). All simulations involving stripe phases utilized a simulation cell (L_x, L_y) commensurate with the stripe structure. Commensurability effects are significant for the stripe phase, which has liquid crystalline-like order and shows significant free energy deviations away from commensurate cell conditions. The microemulsion phase is much softer and does not show significant free energy sensitivity to cell size.

The density profile for pseudospin species α and the momentum distribution were calculated using field configurations:

$$\rho_\alpha[\phi, \phi^*; \mathbf{r}] = \frac{1}{N_\tau} \sum_{j=0}^{N_\tau-1} \phi_{\alpha,j}^*(\mathbf{r}) \phi_{\alpha,j-1}(\mathbf{r}) \quad (3)$$

$$N[\phi, \phi^*; \mathbf{k}] = \frac{A}{N_\tau} \sum_{\alpha} \sum_{j=0}^{N_\tau-1} \tilde{\phi}_{\alpha,j,-\mathbf{k}}^* \tilde{\phi}_{\alpha,j-1,\mathbf{k}} \quad (4)$$

where N_τ is the number of imaginary time points with index j , $\tilde{\phi}$ refers to the Discrete Fourier Transform of ϕ , accessed numerically via Fast Fourier Transform algorithms [14], and $A = L_x L_y$ is the system size (area). Momentum states are labelled by a discrete wavevector $\mathbf{k} = 2\pi(n_x/L_x, n_y/L_y)$, where n_ν

consist of positive and negative integers in each direction. The shifted imaginary time indices emerge naturally during the transformation to a coherent state representation and are required for respecting the causal ordering of ϕ and ϕ^* in imaginary time.

At low temperatures and immiscible conditions ($\eta_g > 1$), the system possesses a stripe ground state with anisotropic superfluidity and broken continuous translational and rotational symmetries, shown in Figure (1a). Superfluid density tensor calculations (see Methods) reveal superfluidity in the direction normal to the striped layers yet significant normal fluid character along the stripes, even at quite low temperatures. For vertically oriented stripes under isotropic SOC, free particle-like excitations appear in the \hat{y} Bogoluibov spectrum [39] and disrupt superfluidity along the stripes. In contrast, the \hat{x} excitation spectrum hosts double gapless bands that signify supersolid character normal to the stripes, which arise from the simultaneously broken $U(1)$ and continuous translational symmetries.

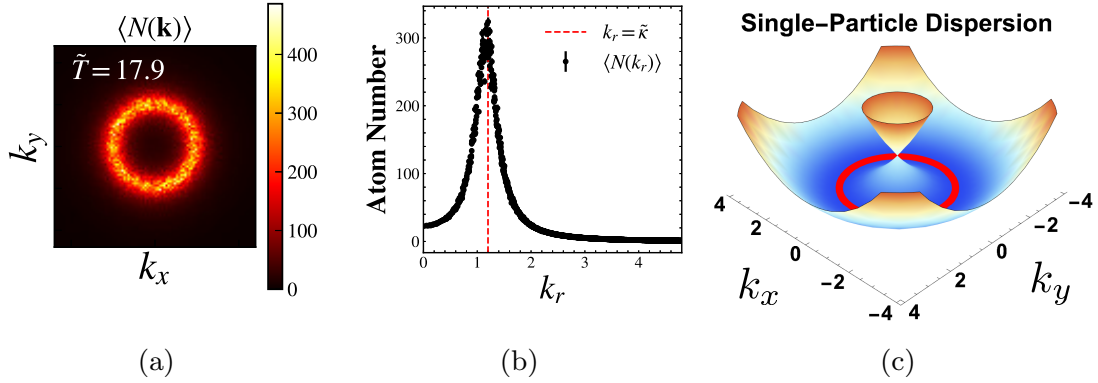


Fig. 2: Momentum distribution and ring motif. **a.** Thermal average momentum state occupation $N(\mathbf{k})$ of the microemulsion with $\langle N \rangle \sim 4.8 \times 10^5$ particles at $\tilde{T} = 17.9$, $\tilde{\kappa} = 1.2$, $\tilde{g} = 0.05$, and $\eta_g = 1.1$ with **b.** angular averaged momentum occupation, showing a peak at $k_r = \tilde{\kappa}$. Error bars are standard errors of the mean, calculated during the Langevin time sample averaging process. **c.** Single-particle dispersion $E_{\pm}(\mathbf{k})$ for isotropic SOC in 2 dimensions. The degenerate energy minima lie on a circle of radius $|\mathbf{k}| = \kappa$, highlighted in red, on the lower branch $E_-(\mathbf{k})$ corresponding to negative helicity. A Dirac point occurs at $\mathbf{k} = \mathbf{0}$ where the positive and negative helicity branches touch.

The stripe phase is characterized by a quasi-condensate that is fragmented into two macroscopically occupied modes in momentum space, which explains the robust $\pi/\tilde{\kappa}$ periodicity of the standing-wave stripe structure. Despite the stripe's apparent smectic character and broken rotational symmetry in our simulations, the finite-temperature stripe phase in the thermodynamic limit should lose long range positional order in the presence of quantum and thermal fluctuations to produce a 2D superfluid nematic [30], in agreement with the Mermin-Wagner theorem. Although we anticipate that the stripes undergo a smectic to nematic transition at $T = 0$, our moderate sized simulation

cells cannot access the genuine nematic except at temperatures just below the transition to the isotropic microemulsion [40]. The appearance of a superfluid nematic at $\tilde{T} > 0$ is analogous to the smectic to nematic transition in classical 2D liquid crystals where phonons and defects destroy smectic translational order at finite temperature [41].

The transition from the stripe to emulsion phase is qualitatively shown via density snapshots at different temperatures: Figure (1) shows the density profiles of the $|\uparrow\rangle$ pseudospin species and shows a clear transition from a quasi-long range ordered smectic to an isotropic, bicontinuous emulsion. The domains have a characteristic width $w \sim \pi/2\tilde{\kappa}$ broadened by thermal fluctuations (Figure (1b), (1c)). This structure reflects a significant occupation of momentum states with wavevector $|\mathbf{k}| = \tilde{\kappa}$, shown in the momentum distribution (Figure (2a)) and suggests a massive fragmentation of the quasi-condensate onto the Rashba dispersion's circular manifold of states (Figure (2c)). This circular momentum distribution presents an appealing experimental signature for the microemulsion phase and could be observed in a time-of-flight cold atom experiment, using either spin-resolved (Stern-Gerlach) or spin-unresolved techniques.

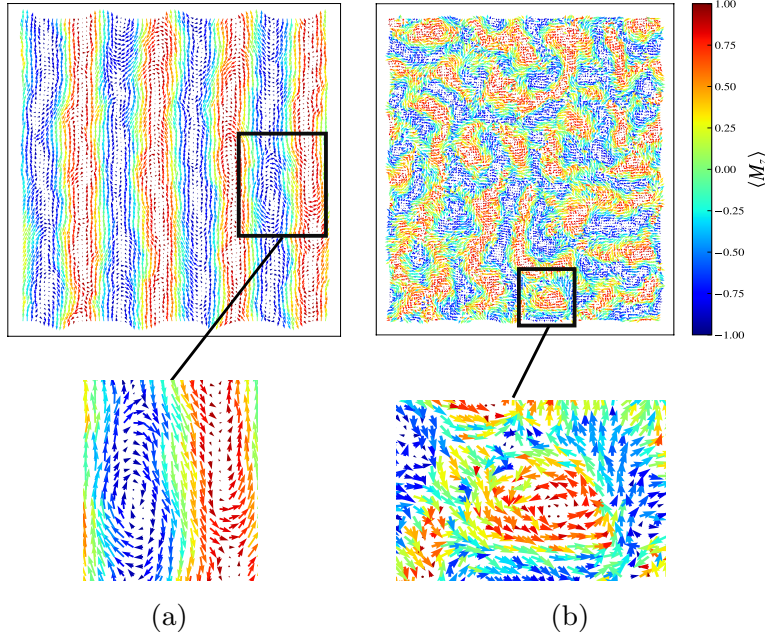


Fig. 3: Pseudospin textures and topological defects. Visualization of the pseudo-magnetization profile $\mathbf{M}(\mathbf{r})$ at $\tilde{\kappa} = 0.4$, $\tilde{g} = 0.05$, and $\eta_g = 1.1$ in **a.** the stripe phase, $\tilde{T} = 1.1$, and **b.** the microemulsion phase, $\tilde{T} = 10.25$. Color bar shows the magnitude of $M_z(\mathbf{r})$. Arrows represent the planar vector $(M_x(\mathbf{r}), M_y(\mathbf{r}))$. Boxed regions are enlarged to show planar pseudospin vortex defects. The plotted local magnetization vector is normalized by the local magnitude $|\mathbf{M}(\mathbf{r})| = \sqrt{M_x^2(\mathbf{r}) + M_y^2(\mathbf{r}) + M_z^2(\mathbf{r})}$. Images were produced after averaging 5 importance-sampled configurations.

The pseudospin real-space density profiles correspond to an underlying \hat{z} antiferromagnetic texture in both the stripe and emulsion phases. The stripe phase is a spin density wave in one direction that resembles spin density waves found in electronic systems [11]. Upon melting, the spin stripes undulate and twist into an isotropic “spin emulsion” structure that resembles bicontinuous microemulsions found in soft matter systems. To study the local pseudospin details, we calculate components of the local magnetization field:

$$M_\nu[\phi, \phi^*; \mathbf{r}] = \frac{1}{N_\tau} \sum_{\alpha\beta} \sum_{j=0}^{N_\tau-1} \phi_{\alpha,j}^*(\mathbf{r}) \sigma_{\alpha\beta}^\nu \phi_{\beta,j-1}(\mathbf{r}) \quad (5)$$

where $\sigma_{\alpha\beta}^\nu$ represents an element of the spin-1/2 Pauli matrix in the ν direction. Both the stripe and microemulsion phases are characterized by strong antiferromagnetic $M_z(\mathbf{r})$ textures shown in Figure (3).

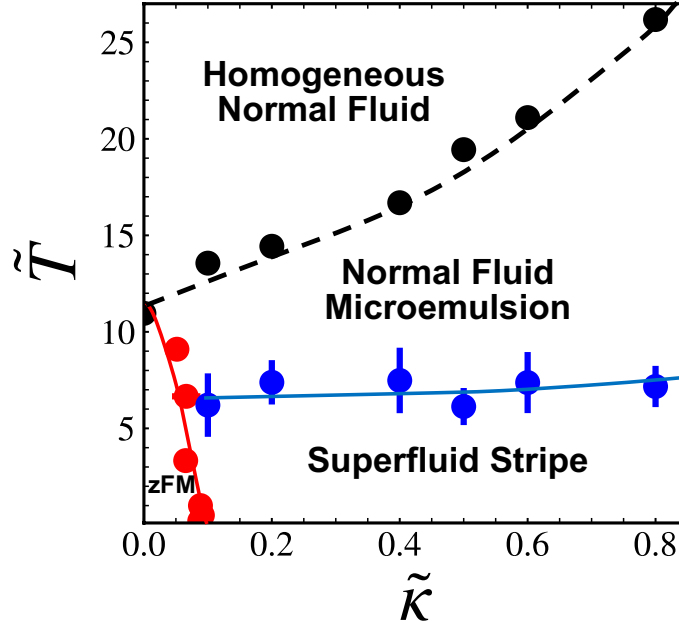


Fig. 4: Finite-temperature phase diagram in the \tilde{T} - $\tilde{\kappa}$ plane. Finite-temperature phase diagram of interacting bosons with isotropic SOC in 2 dimensions, constructed for $\eta_g = 1.1$, $\tilde{g} = 0.05$. Lines are a guide for the eye, and error bars are determined in the Supplementary Information. The blue solid line denotes the Kosterlitz–Thouless-like critical transition, while the red line denotes a first order phase transition into the \hat{z} -Ferromagnet (zFM) phase. The black dashed line depicts a crossover between the spin microemulsion and homogeneous normal fluid.

The stripe and emulsion phase exhibit rich $M_x(\mathbf{r})$ and $M_y(\mathbf{r})$ planar pseudospin textures. The zoomed regions in Figure (3a) and (3b) highlight planar pseudospin vortex defects present throughout both phases. In the stripe phase, full vortices occur within a stripe and appear bound to vortices of opposite

charge in adjacent stripes via domain walls and 1D skyrmions (Figure (3a)); in contrast, vortices in the microemulsion phase appear free and manifest as 2D skyrmions (Figure (3b)). The shift from bound vortex pairs to free vortices across the stripe to microemulsion transition suggests a Kosterlitz–Thouless (KT) picture. These vortices in pseudospin disappear completely upon crossing over at higher temperatures to the paramagnetic normal fluid.

The predicted finite-temperature phase diagram in the \tilde{T} – $\tilde{\kappa}$ plane is shown in Figure (4) for slightly immiscible and isotropic SOC conditions. To observe various thermal transitions, we varied the temperature at fixed $\tilde{\kappa} \geq 0.1$ and monitored the averaged momentum distributions, which revealed three distinct phases, shown in Figures (5a – 5c). Different interaction strengths $\tilde{g} > 0$ and miscibility values $\eta_g > 1$ would shift phase boundaries while leaving the topology of the phase diagram unaltered. The microemulsion emerges as a clear and robust intermediate between the low-temperature ordered stripe superfluid and a high-temperature homogeneous normal fluid.

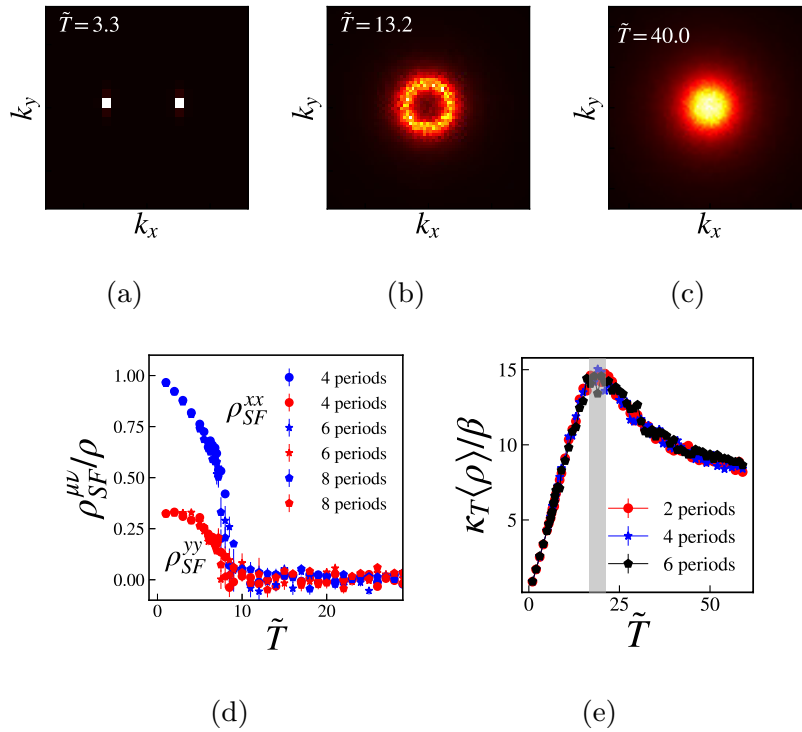


Fig. 5: Finite-temperature phase transitions. Top panel: Momentum distribution $N(\mathbf{k})$ at $\tilde{\kappa} = 0.5$, $\tilde{g} = 0.05$, and $\eta_g = 1.1$ for the **a.** stripe phase at $\tilde{T} = 3.3$, **b.** spin microemulsion phase at $\tilde{T} = 13.2$, and **c.** homogeneous normal fluid at $\tilde{T} = 40.0$. **d.** Superfluid stiffness tensor across the stripe to emulsion thermal phase transition at $\tilde{\kappa} = 0.50$ at various system sizes. The ρ_{SF}^{xx} (ρ_{SF}^{yy}) fraction is shown with blue (red) markers. **e.** Isothermal compressibility at $\tilde{\kappa} = 0.5$ at different system sizes; the universal peak near $\tilde{T} = 19.4$ (gray shading) highlights the crossover from a structured microemulsion to a homogeneous normal fluid. All error bars are standard errors of the mean calculated during the Langevin time sample averaging process.

The microemulsion's appearance at moderate \tilde{T} coincides with a complete loss of superfluidity (Figure (5d)) from the stripe phase, showing characteristics similar to a KT transition. To determine that phase boundary for a given $\tilde{\kappa}$, the superfluid stiffness tensor's diagonal normal component ρ_{SF}^{xx} was tracked with increasing temperature. ρ_{SF}^{xx} declines to zero near the critical stripe melting temperature (Figure (5d)), reminiscent of the finite-size KT transition in conventional 2D superfluids, liquid crystals, and superconductors [42]. To determine the precise critical temperature, we conducted a finite-size scaling analysis (see SI) on ρ_{SF}^{xx} to correct for finite-size errors and estimate the KT transition temperature in the thermodynamic limit. Although the superfluid stiffness parallel to the stripes ρ_{SF}^{yy} shows a similar decline, the normal component ρ_{SF}^{xx} experiences a full variation and serves as a more appropriate measure of the helicity or superfluidity modulus to align with a universal jump quantitatively. All stripe simulations used stripes along the \hat{y} direction in the initial condition to ensure consistency in this anisotropy, and the time scale for rotations in stripe orientation exceed the simulation time. The finite-size analysis suggests a transition mediated by the unbinding of half-vortex phase defects in the nematic superfluid, where the magnitude of the universal jump is modified [30].

At higher temperatures, the spin microemulsion continuously crosses over to a disordered paramagnetic state. This crossover involves overcoming an energy difference $\Delta = E_{-}(\mathbf{k} = \mathbf{0}) - E_{-}(|\mathbf{k}| = \tilde{\kappa})$ between the Dirac point and the circular degenerate manifold, where $\Delta \sim \tilde{\kappa}^2$ (Figure (2c)); this scaling supports the positive curvature of the microemulsion to homogeneous fluid crossover curve observed (Figure (4)). The homogeneous fluid represents a significant occupation of the single-particle branch with positive helicity $E_{+}(\mathbf{k})$ and is supported by the momentum distribution in Figures (5b) and (5c), where the maximum occupation moves from $\mathbf{k} = |\tilde{\kappa}|$ to $\mathbf{k} = \mathbf{0}$ as \tilde{T} increases. This crossover coincides with an anomaly in the 2D isothermal compressibility $\kappa_T = -\frac{1}{A} \frac{dA}{dP}|_T$ (Figure (5e)) that shows no statistically significant finite-size error, suggesting a crossover rather than a critical phase transition with diverging correlation length.

At low SOC strength $\tilde{\kappa} < 0.1$ and low \tilde{T} , the system reduces to a weakly interacting pseudospin-1/2 Bose fluid, where the immiscibility promotes a \hat{z} -Ferromagnet (zFM) superfluid ground state with broken \mathbb{Z}_2 and $U(1)$ symmetries. This state is conveniently probed in the grand canonical ensemble where the system selects a nearly full occupation of either pseudospin state $|\uparrow\rangle$ or $|\downarrow\rangle$ due to a thermodynamic phase coexistence of two homogeneous superfluids with opposing macroscopic pseudospin. The transition between the zFM and the stripe phase was studied via direct calculation of the grand potential Ω for each phase (see SI), where the phase with the lowest grand potential is deemed more thermodynamically stable [43]. Observed jumps in order parameters such as the $\mathbf{k} = \mathbf{0}$ occupation fraction $N_{k=0}/N$ and the integrated \hat{z} -projection of the magnetization $M_z = \int d^2r M_z(\mathbf{r})$ suggest that the phase

transition is first order. The first-order character is confirmed by an observed kink in the grand potential at $\tilde{\kappa}_c$ (see SI).

Next, we discuss the broader implications and significance of our results. Despite a well established literature on liquid crystal systems and their analogues in classical and Fermi quantum systems, they are less well studied and understood in Bose quantum systems. So far, the thermal phase transitions of strongly correlated, bosonic stripe liquid crystal analogues have been studied in lattice boson cold atom systems with hard-core interactions [44] and spin-orbit coupling [45], as well as cold atoms with dipolar interactions [46]. Our study contributes to this growing literature on bosonic stripe liquid crystal analogues and provides the first example of an isotropic, microemulsion intermediate. It is conjectured that the explicit breaking of spin-rotation symmetry by non-zero pseudospin contact interactions can allow for normal fluid magnetic phases [47] like the spin microemulsion reported here.

Beyond this work, the spin microemulsion's circular momentum distribution is reminiscent of other intermediate isotropic phases in condensed matter physics, such as the melting of Dzyaloshinskii–Moriya three-dimensional helimagnets [48], where the transition is characterized as a fluctuation-induced first-order Brazovskii transition. Similarly, the lamellar to isotropic transition in symmetric block copolymers is classified as Brazovskii fluctuation-induced first order in 3D, but the situation changes considerably in 2D and has been classified as Kosterlitz–Thouless [40, 41]. Our work fits well into this context of a KT transition mediated by unbinding topological defects in 2D; however, the finite-temperature stripe phase is complicated by the presence of simultaneous dislocation defects in the stripe patterns, planar pseudospin vortices, and vortices in the superfluid phase. The precise interplay and role of each defect in the KT-like transition is a subject for future study.

The significant occupation of degenerate, low-energy states as well as persistence of \hat{z} -antiferromagnetism suggests that the spin microemulsion retains some residual quantum character from the low-temperature stripe phase, despite losing superfluidity. In this context where the entire continuous circle of degenerate states must be considered, a weak quasi-condensate is present on the $\mathbf{k} = |\kappa|$ circular manifold of low-energy states, representing a superposition of states around the circle reminiscent of the Rashba dispersion. Nevertheless, the spin microemulsion undergoes a continuous crossover into an unstructured, paramagnetic normal fluid, resembling a quantum-classical crossover.

Finally, these results provide insight into longstanding questions regarding the finite-temperature behavior of Rashba bosons and provides an explicit example of severely fragmented (quasi) condensation in a circular flat band, where the number of degenerate single-particle states is greater than the number of atoms in the system [49]. In this case, a singly condensed momentum state is absent and instead a spin-correlated, structured normal fluid phase emerges with a circular manifold of occupied momentum modes. This first computational prediction of an emulsion phase in cold atom systems serves to

highlight a confluence among seemingly disparate fields — soft matter physics, electronic condensed matter physics, and atomic physics.

Methods

Quantum Statistical Mechanics and Field-Theoretic Formalism

In the grand canonical ensemble, the equilibrium theory of interacting pseudospin-1/2 bosons with SOC at finite temperature is described by an action functional:

$$\begin{aligned}
S[\phi, \phi^*] = & \sum_{\alpha} \sum_{j=0}^{N_{\tau}-1} \int d^2r \phi_{\alpha,j}^*(\mathbf{r}) [\phi_{\alpha,j}(\mathbf{r}) - \phi_{\alpha,j-1}(\mathbf{r})] \\
& + \frac{\tilde{\beta}}{N_{\tau}} \sum_{\alpha,\gamma} \sum_{j=0}^{N_{\tau}-1} \int d^2r \phi_{\alpha,j}^*(\mathbf{r}) \hat{\mathcal{K}}_{\alpha,\gamma} \phi_{\gamma,j-1}(\mathbf{r}) \\
& + \frac{\tilde{\beta}\tilde{g}}{2N_{\tau}} \sum_{\alpha,\gamma} \sum_{j=0}^{N_{\tau}-1} \int d^2r \phi_{\alpha,j}^*(\mathbf{r}) \phi_{\gamma,j}^*(\mathbf{r}) (\underline{I} + \eta_g \underline{\sigma}^x)_{\alpha\gamma} \phi_{\gamma,j-1}(\mathbf{r}) \phi_{\alpha,j-1}(\mathbf{r})
\end{aligned} \tag{6}$$

$$\underline{\hat{\mathcal{K}}} = \begin{bmatrix} -\tilde{\nabla}^2 - 1 & -2\tilde{\kappa}[-i\partial_{\tilde{x}} - \partial_{\tilde{y}}] \\ -2\tilde{\kappa}[-i\partial_{\tilde{x}} + \partial_{\tilde{y}}] & -\tilde{\nabla}^2 - 1 \end{bmatrix} \tag{7}$$

where ϕ_{α} and ϕ_{α}^* are complex conjugate coherent state fields with pseudospin index α in the $d+1$ spatial and imaginary time coordinates (\mathbf{r}, τ) , where $d=2$ in this work. Imaginary time $\tau \in [0, \tilde{\beta}]$ has been discretized into N_{τ} points, where the index j labels the imaginary-time slice. Periodic boundary conditions in imaginary time are enforced e.g. $\phi_{\alpha,0}(\mathbf{r}) = \phi_{\alpha,N_{\tau}}(\mathbf{r})$. $\hat{\mathcal{K}}_{\alpha\gamma}$ describes a one-body kinetic energy operator matrix element that contains contributions from SOC with strength $\tilde{\kappa}$. $\partial_{\tilde{x}}$ and $\tilde{\nabla}^2$ indicate a dimensionless spatial derivative and Laplacian, respectively. We take \mathbf{r} as a dimensionless coordinate.

Finite-Temperature Sampling

The field theory of interacting, pseudospin-1/2 bosons with SOC at finite temperature is described by a complex action, and thus requires a sampling method that can overcome the highly oscillatory nature of the integrand. We adopt complex Langevin (CL) sampling [37, 38], which prescribes the following stochastic equations of motion for the coherent state fields in fictitious (Langevin) time t :

$$\begin{aligned}
\frac{\partial}{\partial t} \phi_{\alpha,j}(\mathbf{r}, t) &= -\frac{\delta S[\phi, \phi^*]}{\delta \phi_{\alpha,j}^*(\mathbf{r}, t)} + \eta_{\alpha,j}(\mathbf{r}, t) \\
\frac{\partial}{\partial t} \phi_{\alpha,j}^*(\mathbf{r}, t) &= -\frac{\delta S[\phi, \phi^*]}{\delta \phi_{\alpha,j}(\mathbf{r}, t)} + \eta_{\alpha,j}^*(\mathbf{r}, t)
\end{aligned} \tag{8}$$

where $\eta_{\alpha,j} = \eta_{\alpha,j}^{(1)} + i\eta_{\alpha,j}^{(2)}$ and $\eta_{\alpha,j}^* = \eta_{\alpha,j}^{(1)} - i\eta_{\alpha,j}^{(2)}$ are complex conjugate white noise sources that are built from real noise fields $\eta_{\alpha,j}^{(1)}$ and $\eta_{\alpha,j}^{(2)}$ with the following statistics:

$$\langle \eta_{\alpha,j}^{(\mu)}(\mathbf{r}, t) \rangle = 0$$

$$\langle \eta_{\alpha,j}^{(\mu)}(\mathbf{r}, t) \eta_{\beta,k}^{(\nu)}(\mathbf{r}', t') \rangle = \delta_{\mu,\nu} \delta_{\alpha,\beta} \delta_{j,k} \delta(\mathbf{r} - \mathbf{r}') \delta(t - t')$$

Before fictitious time integration, the coherent state fields are discretized using spectral collocation on a real-space-imaginary-time grid with plane wave basis functions [15]. We choose a number N_x of plane waves in each spatial dimension and N_τ points in the imaginary time contour in order to resolve the coherent state fields sufficiently to reduce space-imaginary time discretization errors below the detectable threshold. For all simulations, we utilize a square simulation cell with a system size $A = L_x L_y$ in two dimensions, where the coherent state fields obey periodic boundary conditions in space and imaginary time. We make use of Fast Fourier Transform algorithms to perform 3-dimensional Fourier transforms to the continuous-time Langevin equations above. The coherent state fields are transformed to \mathbf{k} -space and Matsubara frequencies, where the functional derivatives in Equation (8) are efficiently evaluated and used for numerical time-stepping.

To propagate the Langevin equations in fictitious time, the CL equations are discretized with time step Δt and an exponential-time-differencing (ETD) algorithm is used that ensures numerical stability and weak first-order accuracy during integration, following the approach in reference [14]. We adapt that approach by taking SOC contributions into the explicit portion of the ETD algorithm. The algorithm provides access to mean-field (saddle point) solutions when omitting the stochastic terms in Equation (8), since the coherent state fields will converge to local saddle point solutions at long fictitious times. When running fully-fluctuating complex Langevin simulations, we estimate thermal averaged thermodynamic properties using long fictitious-time sample averages of the physical observables of interest, calculated using field operator functionals. All simulations utilized a discretized numerical time step size of $\Delta t < 0.1$ to eliminate discernible numerical time step bias.

Some simulations performed here use an adaptive time-stepping scheme [15], where the time step Δt is allowed to respond to large forcing events, and is layered on top of the ETD numerical method. In a fixed time-stepping scheme, we calculate thermal averages via arithmetic sample averages, while for an adaptive scheme, we use a weighted sample average to correctly restore importance sampling and estimate thermal averages. In an adaptive scheme, the fields will warm up using a fixed time-stepping scheme for a set number of steps that build average force information. After that initial warmup period, the time step is allowed to respond dynamically to large forces and slow down, preventing instabilities. On average, the adaptive time step fluctuates around the nominal value. The choice of fixed or adaptive time-stepping did not affect any of the quantitative results within statistical errors.

Superfluid Density Calculation

The superfluid density tensor is estimated using the phase twist method [50] $\rho_{\text{SF}}^{xy} = \frac{m}{\hbar^2 A} \frac{\partial^2 \Omega(\mathbf{q})}{\partial q_x \partial q_y} \big|_{\mathbf{q} \rightarrow 0}$, where $\Omega(\mathbf{q})$ is the thermodynamic grand potential after an imposed super-flow proportional to \mathbf{q} . This flow is incorporated via a pseudospin-independent and τ -independent phase shift to each coherent state field via $\phi_\alpha(\mathbf{r}, \tau) \rightarrow \phi_\alpha(\mathbf{r}, \tau) e^{i\mathbf{q} \cdot \mathbf{r}}$. From the fundamental relation $\Omega(\mathbf{q}) = -k_B T \ln(\mathcal{Z}(\mathbf{q}))$, the superfluid density tensor becomes a functional of coherent state field configurations that can be averaged across a Langevin simulation:

$$\rho_{\text{SF}}^{\mu\nu} = \langle \rho \rangle \delta_{\mu\nu} - \frac{2\tilde{\beta}}{A} [\langle \mathcal{P}_\mu \mathcal{P}_\nu \rangle - \langle \mathcal{P}_\mu \rangle \langle \mathcal{P}_\nu \rangle] \quad (9)$$

where $\delta_{\mu\nu}$ is the Kronecker delta, $\rho = (N_\uparrow + N_\downarrow)/A$ is the total particle number density, A is the system size, $\tilde{\beta}$ is the dimensionless inverse temperature, and \mathcal{P}_ν denotes the dimensionless physical momentum field operator in the ν direction, which is a functional of the coherent state fields:

$$\mathcal{P}_\nu[\phi, \phi^*] = \frac{1}{N_\tau} \sum_{j=0}^{N_\tau-1} \sum_{\alpha} \int d^2 r \phi_{\alpha,j}^*(\mathbf{r}) [-i\partial_\nu] \phi_{\alpha,j-1}(\mathbf{r}) - \tilde{\kappa} \int d^2 r M_\nu[\phi, \phi^*; \mathbf{r}] \quad (10)$$

where we have utilized the pseudo-magnetization field operator defined in equation (5). The superfluid density is a rank-2 tensor in $d = 2$ and obeys mass conservation $\rho = \rho_{\text{NF}} + \rho_{\text{SF}}$ where $\rho_{\text{SF}} = \frac{1}{2} \text{Tr}[\rho_{\text{SF}}]$.

Isothermal Compressibility Calculation

In the grand canonical ensemble, the isothermal compressibility can be readily accessed via the population variance of the total particle number [15]:

$$\kappa_T = \beta A \left[\frac{\langle N^2 \rangle}{\langle N \rangle^2} - 1 \right] \quad (11)$$

where the total particle number N can be accessed via the density field operator in equation (3) through numerical spatial integration over the system area and a summation over both pseudospin species:

$$N[\phi, \phi^*] = \sum_{\alpha} \int d^2 r \rho_{\alpha}[\phi, \phi^*; \mathbf{r}]$$

Supplementary information. Supplementary information is available for this paper.

Acknowledgments. The authors thank Matthew Fisher and David Weld for helpful discussions. This work was enabled by field-theoretic simulation tools developed under support from the National Science Foundation (CMMT Program, DMR-2104255). Use was made of computational facilities purchased with funds from the NSF (CNS-1725797) and administered by the Center for Scientific Computing (CSC). The CSC is supported by the California NanoSystems Institute and the Materials Research Science and Engineering Center (MRSEC; NSF DMR 1720256) at UC Santa Barbara. E.C.M acknowledges support from a Mitsubishi Chemical Fellowship, and L.B. acknowledges support from the DOE, Office of Science, Basic Energy Sciences under Award No. DE-FG02-08ER46524.

Declarations

Code Availability

The computer code used to produce simulation data is available for license through the Complex Fluids Design Consortium (CFDC) at the University of California Santa Barbara, <https://www.mrl.ucsb.edu/research/complex-fluids-design-consortium>.

Authors' contributions

Simulation runs and data analysis were performed by E.C.M. under the guidance of K.T.D., G.H.F., and L.B. Simulation code was developed by K.T.D. and E.C.M. Theoretical methods were developed by K.T.D., E.C.M., and G.H.F. Physical interpretation and conclusions were provided by E.C.M., K.T.D., G.H.F., and L.B. The manuscript was prepared by E.C.M. with input from all co-authors.

Funding

See acknowledgements.

Data Availability

Data is available upon reasonable request to the corresponding author.

Competing Interests

The authors declare no competing interests.

Consent for Publication

Not applicable

Consent to Participate

Not applicable

Ethics Approval

Not applicable

References

- [1] Lee, D. D., Chen, S. H., Majkrzak, C. F. & Satija, S. K. Bulk and surface correlations in a microemulsion. *Physical Review E* **52** (1), R29–R32 (1995). URL <https://link.aps.org/doi/10.1103/PhysRevE.52.R29>. <https://doi.org/10.1103/PhysRevE.52.R29>, publisher: American Physical Society .
- [2] Guo, S. *et al.* All-Aqueous Bicontinuous Structured Liquid Crystal Emulsion through Intraphase Trapping of Cellulose Nanoparticles. *Biomacromolecules* **24** (1), 367–376 (2023). URL <https://doi.org/10.1021/acs.biomac.2c01177>. <https://doi.org/10.1021/acs.biomac.2c01177>, publisher: American Chemical Society .
- [3] Bonelli, F. *et al.* Lamellar ordering, droplet formation and phase inversion in exotic active emulsions. *Scientific Reports* **9** (1), 2801 (2019). URL <https://www.nature.com/articles/s41598-019-39190-6>. <https://doi.org/10.1038/s41598-019-39190-6> .
- [4] Huang, C. *et al.* Bicontinuous structured liquids with sub-micrometre domains using nanoparticle surfactants. *Nature Nanotechnology* **12** (11), 1060–1063 (2017). URL <https://www.nature.com/articles/nnano.2017.182>. <https://doi.org/10.1038/nnano.2017.182>, number: 11 Publisher: Nature Publishing Group .
- [5] De Gennes, P. G. & Taupin, C. Microemulsions and the flexibility of oil/water interfaces. *The Journal of Physical Chemistry* **86** (13), 2294–2304 (1982). URL <https://doi.org/10.1021/j100210a011>. <https://doi.org/10.1021/j100210a011>, publisher: American Chemical Society .
- [6] Clause, M., Peyrelasse, J., Heil, J., Boned, C. & Lagourette, B. Bicontinuous structure zones in microemulsions. *Nature* **293** (5834), 636–638 (1981). URL <https://www.nature.com/articles/293636a0>. <https://doi.org/10.1038/293636a0>, number: 5834 Publisher: Nature Publishing Group .
- [7] Bates, F. S. *et al.* Polymeric Bicontinuous Microemulsions. *Physical Review Letters* **79** (5), 849–852 (1997). URL <https://link.aps.org/doi/10.1103/PhysRevLett.79.849>. <https://doi.org/10.1103/PhysRevLett.79.849>, publisher: American Physical Society .
- [8] Spencer, R. K. W. & Matsen, M. W. Coexistence of Polymeric Microemulsion with Homopolymer-Rich Phases. *Macromolecules* **54** (3), 1329–1337 (2021). URL <https://pubs.acs.org/doi/10.1021/acs.macromol.0c02668>. <https://doi.org/10.1021/acs.macromol.0c02668> .

- [9] Radzihovsky, L. & Vishwanath, A. Quantum Liquid Crystals in an Imbalanced Fermi Gas: Fluctuations and Fractional Vortices in Larkin-Ovchinnikov States. *Physical Review Letters* **103** (1), 010404 (2009). URL <https://link.aps.org/doi/10.1103/PhysRevLett.103.010404>. <https://doi.org/10.1103/PhysRevLett.103.010404> .
- [10] Berg, E., Fradkin, E. & Kivelson, S. A. Charge-4e superconductivity from pair-density-wave order in certain high-temperature superconductors. *Nature Physics* **5** (11), 830–833 (2009). URL <https://www.nature.com/articles/nphys1389>. <https://doi.org/10.1038/nphys1389>, number: 11 Publisher: Nature Publishing Group .
- [11] Sun, K., Fregoso, B. M., Lawler, M. J. & Fradkin, E. Fluctuating stripes in strongly correlated electron systems and the nematic-smectic quantum phase transition. *Physical Review B* **78** (8), 085124 (2008). URL <https://link.aps.org/doi/10.1103/PhysRevB.78.085124>. <https://doi.org/10.1103/PhysRevB.78.085124>, publisher: American Physical Society .
- [12] Spivak, B. & Kivelson, S. A. Transport in two dimensional electronic micro-emulsions. *Annals of Physics* **321** (9), 2071–2115 (2006). URL <https://www.sciencedirect.com/science/article/pii/S0003491605002654>. <https://doi.org/10.1016/j.aop.2005.12.002> .
- [13] Spivak, B. & Kivelson, S. A. Phases intermediate between a two-dimensional electron liquid and Wigner crystal. *Physical Review B* **70** (15), 155114 (2004). URL <https://link.aps.org/doi/10.1103/PhysRevB.70.155114>. <https://doi.org/10.1103/PhysRevB.70.155114> .
- [14] Delaney, K. T., Orland, H. & Fredrickson, G. H. Numerical Simulation of Finite-Temperature Field Theory for Interacting Bosons. *Physical Review Letters* **124** (7), 070601 (2020). URL <https://link.aps.org/doi/10.1103/PhysRevLett.124.070601>. <https://doi.org/10.1103/PhysRevLett.124.070601>, publisher: American Physical Society .
- [15] Fredrickson, G. H. & Delaney, K. T. *Field-Theoretic Simulations in Soft Matter and Quantum Fluids* International Series of Monographs on Physics (Oxford University Press, Oxford, New York, 2023).
- [16] Lin, Y.-J., Jiménez-García, K. & Spielman, I. B. Spin-orbit-coupled Bose-Einstein condensates. *Nature* **471** (7336), 83–86 (2011). URL <https://www.nature.com/articles/nature09887>. <https://doi.org/10.1038/nature09887>, number: 7336 Publisher: Nature Publishing Group .
- [17] Kamehchi, M. A., Qu, C., Mossman, M. E., Zhang, C. & Engels, P. Spin-momentum coupled Bose-Einstein condensates with lattice band pseudospins. *Nature Communications* **7** (1), 10867 (2016). URL <https://www.nature.com/articles/ncomms10867>. <https://doi.org/10.1038/ncomms10867> .

- [10.1038/ncomms10867](https://doi.org/10.1038/ncomms10867), number: 1 Publisher: Nature Publishing Group .
- [18] Ji, S.-C. *et al.* Experimental determination of the finite-temperature phase diagram of a spin-orbit coupled Bose gas. *Nature Physics* **10** (4), 314–320 (2014). URL <https://www.nature.com/articles/nphys2905>. <https://doi.org/10.1038/nphys2905>, number: 4 Publisher: Nature Publishing Group .
 - [19] Hamner, C., Zhang, Y., Khamsehchi, M., Davis, M. J. & Engels, P. Spin-Orbit-Coupled Bose-Einstein Condensates in a One-Dimensional Optical Lattice. *Physical Review Letters* **114** (7), 070401 (2015). URL <https://link.aps.org/doi/10.1103/PhysRevLett.114.070401>. <https://doi.org/10.1103/PhysRevLett.114.070401>, publisher: American Physical Society .
 - [20] Manchon, A., Koo, H. C., Nitta, J., Frolov, S. M. & Duine, R. A. New perspectives for Rashba spin-orbit coupling. *Nature Materials* **14** (9), 871–882 (2015). URL <https://www.nature.com/articles/nmat4360>. <https://doi.org/10.1038/nmat4360>, number: 9 Publisher: Nature Publishing Group .
 - [21] Li, J.-R. *et al.* A stripe phase with supersolid properties in spin-orbit-coupled Bose-Einstein condensates. *Nature* **543** (7643), 91–94 (2017). URL <https://www.nature.com/articles/nature21431>. <https://doi.org/10.1038/nature21431>, number: 7643 Publisher: Nature Publishing Group .
 - [22] Bersano, T. M. *et al.* Experimental realization of a long-lived striped Bose-Einstein condensate induced by momentum-space hopping. *Physical Review A* **99** (5), 051602 (2019). URL <https://link.aps.org/doi/10.1103/PhysRevA.99.051602>. <https://doi.org/10.1103/PhysRevA.99.051602>, publisher: American Physical Society .
 - [23] Bychkov, Y. A. & Rashba, E. I. Oscillatory effects and the magnetic susceptibility of carriers in inversion layers. *Journal of Physics C: Solid State Physics* **17** (33), 6039 (1984). URL <https://dx.doi.org/10.1088/0022-3719/17/33/015>. <https://doi.org/10.1088/0022-3719/17/33/015> .
 - [24] Michiardi, M. *et al.* Optical manipulation of Rashba-split 2-dimensional electron gas. *Nature Communications* **13** (1), 3096 (2022). URL <https://www.nature.com/articles/s41467-022-30742-5>. <https://doi.org/10.1038/s41467-022-30742-5>, number: 1 Publisher: Nature Publishing Group .
 - [25] Wu, K. *et al.* Two-Dimensional Giant Tunable Rashba Semiconductors with Two-Atom-Thick Buckled Honeycomb Structure. *Nano Letters* **21** (1), 740–746 (2021). URL <https://doi.org/10.1021/acs.nanolett.0c04429>. <https://doi.org/10.1021/acs.nanolett.0c04429>, publisher: American Chemical Society .

- [26] Valdés-Curiel, A., Trypogeorgos, D., Liang, Q.-Y., Anderson, R. P. & Spielman, I. B. Topological features without a lattice in Rashba spin-orbit coupled atoms. *Nature Communications* **12** (1), 593 (2021). URL <https://www.nature.com/articles/s41467-020-20762-4>. <https://doi.org/10.1038/s41467-020-20762-4>, number: 1 Publisher: Nature Publishing Group .
- [27] Campbell, D. L. & Spielman, I. B. Rashba realization: Raman with RF. *New Journal of Physics* **18** (3), 033035 (2016). URL <https://dx.doi.org/10.1088/1367-2630/18/3/033035>. <https://doi.org/10.1088/1367-2630/18/3/033035>, publisher: IOP Publishing .
- [28] Kawasaki, E. & Holzmann, M. Finite-temperature phases of two-dimensional spin-orbit-coupled bosons. *Physical Review A* **95** (5), 051601 (2017). URL <https://link.aps.org/doi/10.1103/PhysRevA.95.051601>. <https://doi.org/10.1103/PhysRevA.95.051601>, publisher: American Physical Society .
- [29] Sinha, S., Nath, R. & Santos, L. Trapped Two-Dimensional Condensates with Synthetic Spin-Orbit Coupling. *Physical Review Letters* **107** (27), 270401 (2011). URL <https://link.aps.org/doi/10.1103/PhysRevLett.107.270401>. <https://doi.org/10.1103/PhysRevLett.107.270401>, publisher: American Physical Society .
- [30] Jian, C.-M. & Zhai, H. Paired superfluidity and fractionalized vortices in systems of spin-orbit coupled bosons. *Physical Review B* **84** (6), 060508 (2011). URL <https://link.aps.org/doi/10.1103/PhysRevB.84.060508>. <https://doi.org/10.1103/PhysRevB.84.060508>, publisher: American Physical Society .
- [31] Ozawa, T. & Baym, G. Condensation Transition of Ultracold Bose Gases with Rashba Spin-Orbit Coupling. *Physical Review Letters* **110** (8), 085304 (2013). URL <https://link.aps.org/doi/10.1103/PhysRevLett.110.085304>. <https://doi.org/10.1103/PhysRevLett.110.085304>, publisher: American Physical Society .
- [32] Stanescu, T. D., Anderson, B. & Galitski, V. Spin-orbit coupled Bose-Einstein condensates. *Physical Review A* **78** (2), 023616 (2008). URL <https://link.aps.org/doi/10.1103/PhysRevA.78.023616>. <https://doi.org/10.1103/PhysRevA.78.023616> .
- [33] Sedrakyan, T. A., Kamenev, A. & Glazman, L. I. Composite fermion state of spin-orbit-coupled bosons. *Physical Review A* **86** (6), 063639 (2012). URL <https://link.aps.org/doi/10.1103/PhysRevA.86.063639>. <https://doi.org/10.1103/PhysRevA.86.063639>, publisher: American Physical Society .

- [34] Goldman, N., Juzeliūnas, G., Öhberg, P. & Spielman, I. B. Light-induced gauge fields for ultracold atoms. *Reports on Progress in Physics* **77** (12), 126401 (2014). URL <https://iopscience.iop.org/article/10.1088/0034-4885/77/12/126401/meta>. <https://doi.org/10.1088/0034-4885/77/12/126401>, publisher: IOP Publishing .
- [35] Fetter, A. L. & Walecka, J. D. *Quantum Theory of Many-Particle Systems* (Courier Corporation, 2012). Google-Books-ID: t5_DAgAAQBAJ.
- [36] Negele, J. W. & Orland, H. *Quantum Many-particle Systems* (Basic Books, 1988). Google-Books-ID: EV8sAAAAYAAJ.
- [37] Parisi, G. On complex probabilities. *Physics Letters B* **131** (4), 393–395 (1983). URL <https://www.sciencedirect.com/science/article/pii/0370269383905257>. [https://doi.org/10.1016/0370-2693\(83\)90525-7](https://doi.org/10.1016/0370-2693(83)90525-7) .
- [38] Klauder, J. R. A Langevin approach to fermion and quantum spin correlation functions. *Journal of Physics A: Mathematical and General* **16** (10), L317 (1983). URL <https://dx.doi.org/10.1088/0305-4470/16/10/001>. <https://doi.org/10.1088/0305-4470/16/10/001> .
- [39] Liao, R. Searching for Supersolidity in Ultracold Atomic Bose Condensates with Rashba Spin-Orbit Coupling. *Physical Review Letters* **120** (14), 140403 (2018). URL <https://link.aps.org/doi/10.1103/PhysRevLett.120.140403>. <https://doi.org/10.1103/PhysRevLett.120.140403> .
- [40] Hammond, M. R., Cochran, E., Fredrickson, G. H. & Kramer, E. J. Temperature Dependence of Order, Disorder, and Defects in Laterally Confined Diblock Copolymer Cylinder Monolayers. *Macromolecules* **38** (15), 6575–6585 (2005). URL <https://doi.org/10.1021/ma050479l>. <https://doi.org/10.1021/ma050479l>, publisher: American Chemical Society .
- [41] Toner, J. & Nelson, D. R. Smectic, cholesteric, and Rayleigh-Benard order in two dimensions. *Physical Review B* **23** (1), 316–334 (1981). URL <https://link.aps.org/doi/10.1103/PhysRevB.23.316>. <https://doi.org/10.1103/PhysRevB.23.316>, publisher: American Physical Society .
- [42] Nelson, D. R. & Kosterlitz, J. M. Universal Jump in the Superfluid Density of Two-Dimensional Superfluids. *Physical Review Letters* **39** (19), 1201–1205 (1977). URL <https://link.aps.org/doi/10.1103/PhysRevLett.39.1201>. <https://doi.org/10.1103/PhysRevLett.39.1201>, publisher: American Physical Society .
- [43] Fredrickson, G. H. & Delaney, K. T. Direct free energy evaluation of classical and quantum many-body systems via field-theoretic simulation. *Proceedings of the National Academy of Sciences* **119** (18), e2201804119 (2022). URL <https://www.pnas.org/doi/full/10.1073/pnas.2201804119>.

- <https://doi.org/10.1073/pnas.2201804119>, publisher: Proceedings of the National Academy of Sciences .
- [44] Schmid, G. & Troyer, M. Melting of Bosonic Stripes. *Physical Review Letters* **93** (6), 067003 (2004). URL <https://link.aps.org/doi/10.1103/PhysRevLett.93.067003>. <https://doi.org/10.1103/PhysRevLett.93.067003>, publisher: American Physical Society .
 - [45] Hickey, C. & Paramakanti, A. Thermal Phase Transitions of Strongly Correlated Bosons with Spin-Orbit Coupling. *Physical Review Letters* **113** (26), 265302 (2014). URL <https://link.aps.org/doi/10.1103/PhysRevLett.113.265302>. <https://doi.org/10.1103/PhysRevLett.113.265302> .
 - [46] Bombín, R., Mazzanti, F. & Boronat, J. Berezinskii-Kosterlitz-Thouless transition in two-dimensional dipolar stripes. *Physical Review A* **100** (6), 063614 (2019). URL <https://link.aps.org/doi/10.1103/PhysRevA.100.063614>. <https://doi.org/10.1103/PhysRevA.100.063614> .
 - [47] Radić, J., Natu, S. S. & Galitski, V. Stoner Ferromagnetism in a Thermal Pseudospin- 1 / 2 Bose Gas. *Physical Review Letters* **113** (18), 185302 (2014). URL <https://link.aps.org/doi/10.1103/PhysRevLett.113.185302>. <https://doi.org/10.1103/PhysRevLett.113.185302> .
 - [48] Phys. Rev. B 87, 134407 (2013) - Fluctuation-induced first-order phase transition in Dzyaloshinskii-Moriya helimagnets. URL <https://journals.aps.org/prb/abstract/10.1103/PhysRevB.87.134407>.
 - [49] Mueller, E. J., Ho, T.-L., Ueda, M. & Baym, G. Fragmentation of Bose-Einstein condensates. *Physical Review A* **74** (3), 033612 (2006). URL <https://link.aps.org/doi/10.1103/PhysRevA.74.033612>. <https://doi.org/10.1103/PhysRevA.74.033612>, publisher: American Physical Society .
 - [50] Subaşı, A. L. & Iskin, M. Quantum-geometric perspective on spin-orbit-coupled Bose superfluids. *Physical Review A* **105** (2), 023301 (2022). URL <https://link.aps.org/doi/10.1103/PhysRevA.105.023301>. <https://doi.org/10.1103/PhysRevA.105.023301> .

Supplementary Information: Emergence of a spin microemulsion in spin-orbit coupled Bose-Einstein condensates

Ethan C. McGarrigle¹, Kris T. Delaney², Leon Balents³
and Glenn H. Fredrickson^{1,2,4*}

¹Department of Chemical Engineering, University of California,
Santa Barbara, 93106, California, USA.

²Materials Research Laboratory, University of California, Santa
Barbara, 93106, California, USA.

³Kavli Institute for Theoretical Physics, University of California,
Santa Barbara, 93106, California, USA.

^{4*}Department of Materials, University of California, Santa
Barbara, 93106, California, USA.

*Corresponding author(s). E-mail(s): ghf@ucsb.edu;
Contributing authors: emcgarrigle@ucsb.edu;
kdelaney@mrl.ucsb.edu; balents@ucsb.edu;

Determining the Stripe to zFM Transition

The z-Ferromagnet (zFM) phase consists of two degenerate phases ($|\uparrow\rangle$ and $|\downarrow\rangle$ superfluids) that are macroscopically phase separated but in phase-coexistence equilibrium. In pseudospin mixtures where each particle number N_α is held fixed, there will be a sharp, dividing interface between the coexisting superfluids. Comparisons between a two-phase superfluid and a periodic stripe phase would be difficult in canonical ensemble simulations with particle number N_α fixed. Free energy comparisons would require large simulation cells to prove the two-phase superfluid lacks periodicity while showing diminishing free energy contributions from the interface. A more efficient method to probe the zFM phase is to use the grand canonical ensemble, where the chemical potential μ of each pseudospin species is equal and fixed. There, the system relaxes to a configuration that minimizes the natural thermodynamic potential — the grand potential Ω — by selecting either a pure $|\uparrow\rangle$ or $|\downarrow\rangle$ homogeneous superfluid state without any interface.

To study the stripe to zFM phase transition, we develop an extension to reference [1] to calculate the grand potential for each phase in the metastable window where the zFM and stripe phases coexist. While thermodynamic potentials are cumbersome to access in particle simulations, field-theoretic representations provide direct access to operators that can be averaged in a field-theoretic simulation to yield free energy estimates [1]. Here we detail how to estimate the grand potential in field theoretic simulations and provide a brief summary of our methods.

The grand potential is defined using standard thermodynamic relations [2] for a two-dimensional system with size (area) A :

$$\begin{aligned}\Omega(\mu, A, T) &= F - \mu N = E - TS - \mu \sum_{\alpha} N_{\alpha} \\ d\Omega &= -SdT - PdA - \sum_{\alpha} N_{\alpha} d\mu \\ P &= - \left(\frac{\partial \Omega}{\partial A} \right)_{\mu, T}\end{aligned}\tag{1}$$

where F is the Helmholtz free energy and μ is the chemical potential for both pseudospin boson species. For homogeneous systems, the grand potential is both extensive and a function of only one extensive quantity (system size), therefore Ω must be a homogeneous function of order 1 in the system size A and can thus be expressed $\Omega(\mu, A, T) = A \left. \frac{\partial \Omega}{\partial A} \right|_{T, \mu}$. From the differential form in equation (1), the area derivative is identified readily as the pressure, and the grand potential can be evaluated for a homogeneous system, in agreement with reference [2]:

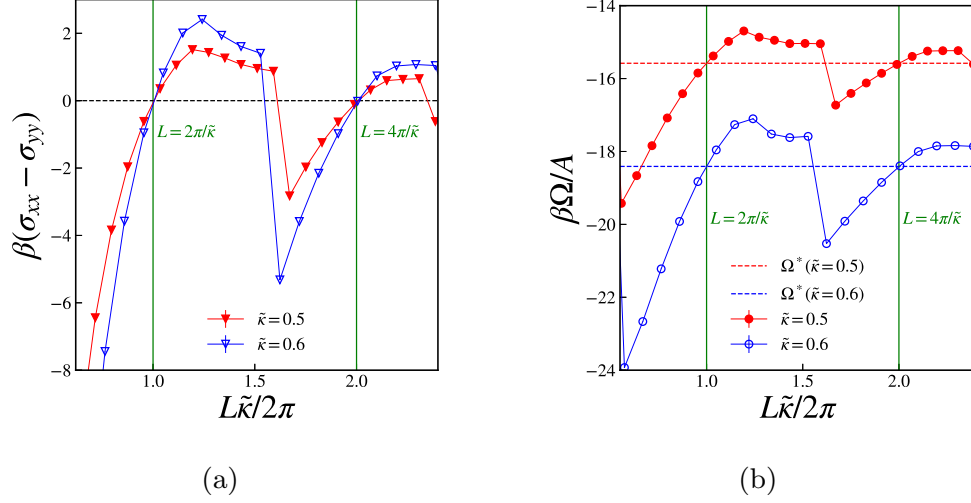


Fig. 1: Stripe phase commensurability analysis for $\tilde{T} = 1.0$, $\eta_g = 1.1$, $\tilde{g} = 0.05$, and two SOC coupling strengths $\tilde{\kappa} = 0.5$ and $\tilde{\kappa} = 0.6$. **a.** Difference in cell stress tensor diagonal components for different simulation cell sizes L . Isotropic stress conditions occur when the diagonal stress difference intersects the dashed black line, which corresponds precisely to $L^* = \frac{2\pi n}{\tilde{\kappa}}$. **b.** Intensive grand potential as a function of system size. The intensive grand potential $\beta\Omega^*(\tilde{\kappa})/A$ values for $\tilde{\kappa} = 0.5$ and $\tilde{\kappa} = 0.6$ at commensurate conditions are shown with dashed horizontal lines. Sharp changes occur near $L\tilde{\kappa}/2\pi = 1.5$ and correspond to the system adding another set of stripes to accommodate the larger cell size. Error bars are standard errors of the mean determined in the Langevin sampling averaging process and are smaller than the symbol size.

$$\Omega = -PA \quad (2)$$

Now, we extend the argument to the case of an ordered, *periodic* mesophase, with direct application to the superfluid stripe phase in this work. For stripe systems that are scaled based on the unit cell that is commensurate with the stripe's periodicity, all intensive properties are invariant by definition. Therefore, the above arguments for a homogeneous system apply and Ω must be a homogeneous function of order 1 as long as the simulation cell is commensurate with the stripe's periodicity $\frac{2\pi n}{\tilde{\kappa}}$ for all positive integers n . As a result, we calculate Ω using equation (2) for both a periodic stripe and a spatially homogeneous zFM phase.

To link macroscopic thermodynamics with the microscopic details of the system, we utilize the definition of the grand potential from quantum statistical mechanics $\Omega(\mu, A, T) = -\frac{1}{\beta} \ln(\mathcal{Z})$ where \mathcal{Z} denotes the grand canonical partition function and $\beta = 1/k_B T$. Our simulations naturally represent conditions of fixed μ and T , so the pressure provides thermodynamic information related to the grand potential. With this link between the grand potential and the grand partition function, we determine a pressure operator functional in the grand canonical ensemble via the definition of pressure in equation (1):

$$P = \frac{1}{\beta} \frac{\partial \ln(\mathcal{Z})}{\partial A} = -\frac{1}{\beta} \left\langle \frac{\partial S[\phi, \phi^*]}{\partial A} \right\rangle_{\mu, T} \quad (3)$$

where the area derivative is determined analytically using a procedure outlined in reference [1], yielding a pressure field operator functional:

$$\begin{aligned} \beta P[\phi, \phi^*] = & \frac{-\tilde{\beta}}{N_\tau A} \sum_{j=0}^{N_\tau-1} \sum_{\alpha, \gamma} \int d^2 r \phi_{\alpha, j}^*(\mathbf{r}) \frac{\partial \hat{\mathcal{K}}_{\alpha, \gamma}}{\partial A} \phi_{\gamma, j-1}(\mathbf{r}) \\ & + \frac{\tilde{\beta} \tilde{g}}{2N_\tau A} \sum_{\alpha, \gamma} \sum_{j=0}^{N_\tau-1} \int d^2 r \phi_{\alpha, j}^*(\mathbf{r}) \phi_{\gamma, j}^*(\mathbf{r}) (\underline{I} + \eta_g \underline{\sigma}^x)_{\alpha\gamma} \phi_{\gamma, j-1}(\mathbf{r}) \phi_{\alpha, j-1}(\mathbf{r}) \end{aligned} \quad (4)$$

$$\frac{\partial \hat{\mathcal{K}}}{\partial A} = \begin{bmatrix} \tilde{\nabla}^2 & -\tilde{\kappa}[i\partial_{\tilde{x}} + \partial_{\tilde{y}}] \\ -\tilde{\kappa}[i\partial_{\tilde{x}} - \partial_{\tilde{y}}] & \tilde{\nabla}^2 \end{bmatrix} \quad (5)$$

From a thermal-averaged pressure, we determine a dimensionless grand potential using $\beta\Omega = -\langle\beta P\rangle A$, where the thermal average is evaluated using a sample average over Langevin time as described in the Methods section of the main text.

Before comparing the grand potentials of each phase, we performed a commensurability analysis to ensure the stripe structures were commensurate with the simulation cell. The commensurate cell size was determined using a cell stress analysis following the method outlined in reference [1] for structured fluids. An excess cell stress operator is derived by quantifying changes in the intensive grand potential with respect to the cell dimensions at constant chemical potential and temperature:

$$\beta \underline{\sigma} = \underline{h} \frac{\partial(\frac{\beta\Omega_{\text{ex}}}{A})}{\partial \underline{h}} \Big|_{\mu, T} = \frac{1}{A} \left\langle \frac{\partial S}{\partial \underline{h}} \right\rangle_{\mu, T} \underline{h}$$

where Ω_{ex} is the excess grand potential and \underline{h} is a symmetric and diagonal cell tensor with $h_{xx} = L_x$, $h_{yy} = L_y$ and $h_{xy} = h_{yx} = 0$. The diagonal components of the dimensionless excess stress in the ν direction are

$$\begin{aligned} \beta \sigma_{\nu\nu}[\phi, \phi^*] = & \frac{2\tilde{\beta}}{N_\tau A} \sum_{j=0}^{N_\tau-1} \sum_{\alpha, \gamma} \int d^2 r \phi_{\alpha, j}^*(\mathbf{r}) \frac{\partial \hat{\mathcal{K}}_{\alpha, \gamma}}{\partial L_\nu} \phi_{\gamma, j-1}(\mathbf{r}) \\ & - \frac{\tilde{\beta} \tilde{g}}{2N_\tau A} \sum_{\alpha, \gamma} \sum_{j=0}^{N_\tau-1} \int d^2 r \phi_{\alpha, j}^*(\mathbf{r}) \phi_{\gamma, j}^*(\mathbf{r}) (\underline{I} + \eta_g \underline{\sigma}^x)_{\alpha\gamma} \phi_{\gamma, j-1}(\mathbf{r}) \phi_{\alpha, j-1}(\mathbf{r}) \end{aligned} \quad (6)$$

$$\frac{\partial \hat{\mathcal{K}}}{\partial L_x} = \begin{bmatrix} \partial_{\tilde{x}}^2 & -i\tilde{\kappa}\partial_{\tilde{x}} \\ -i\tilde{\kappa}\partial_{\tilde{x}} & \partial_{\tilde{x}}^2 \end{bmatrix} \quad \frac{\partial \hat{\mathcal{K}}}{\partial L_y} = \begin{bmatrix} \partial_{\tilde{y}}^2 & -\tilde{\kappa}\partial_{\tilde{y}} \\ \tilde{\kappa}\partial_{\tilde{y}} & \partial_{\tilde{y}}^2 \end{bmatrix}$$

The cell stress tensor $\underline{\sigma}$ becomes isotropic at the commensurate cell size for periodic stripe phases, so we vary the cell length L for vertically oriented stripe structures and monitor the cell stress tensor's diagonal components σ_{xx} and σ_{yy} . We find in Figure (1a) that the commensurate cell length is $L^* = 2\pi n/\tilde{\kappa}$ for a choice of $\tilde{\kappa}$. Figure (1b) shows that the intensive grand potential is invariant to the number of stripes n at the commensurate cell conditions $L = L^*$. For all simulations of the stripe superfluid, we use a square cell $(L_x, L_y) = (L^*, L^*)$ that is commensurate with a vertical stripe structure determined by this analysis. Furthermore, Figure (1b) shows significant grand potential variations are observed for ill-sized simulation cells and illustrates the importance of simulating stripe phases in commensurate cells.

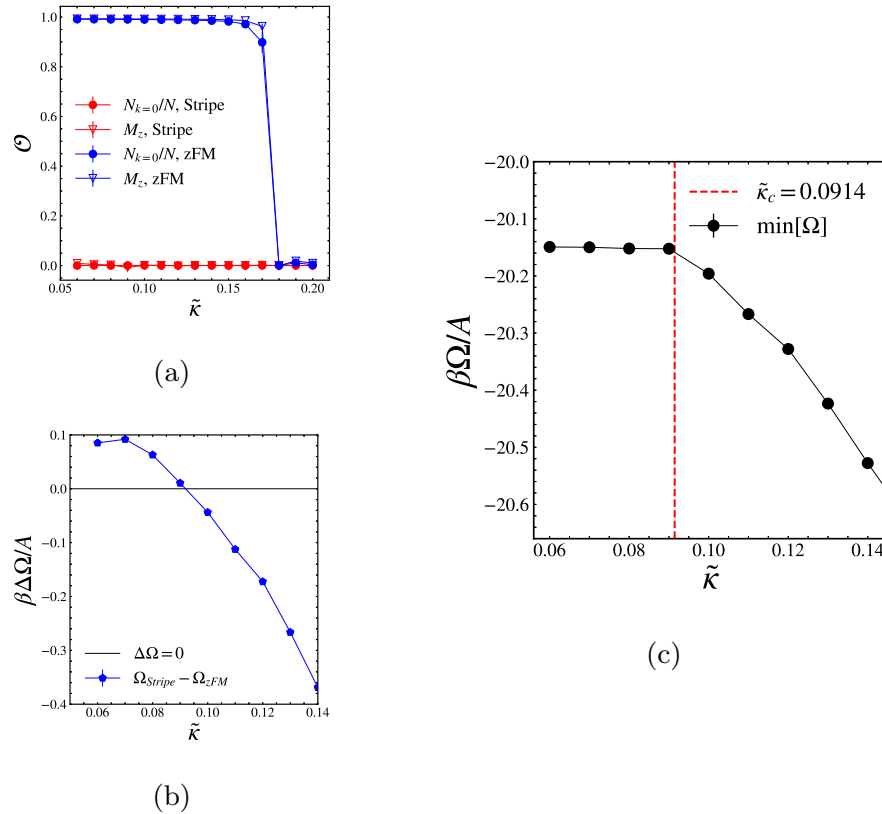


Fig. 2: First order stripe to zFM transition at $\tilde{T} = 0.5$, $\eta_g = 1.1$, $\tilde{g} = 0.05$.
a. The integrated \hat{z} magnetization and $\mathbf{k} = \mathbf{0}$ occupation fraction plotted at different $\tilde{\kappa}$ for the stripe and zFM phases. The zFM phase becomes unstable near $\tilde{\kappa} > 0.17$, where the order parameters jump from 1 to 0, characteristic of a first order transition.
b. Intensive grand potential difference between the zFM and stripe phases. The crossing point with the solid black line determines the phase boundary $\tilde{\kappa}_c$ SOC point.
c. Grand potential $\Omega(\tilde{\kappa})$ plotted using values from the phase with the lower grand potential. The kink is evident near $\tilde{\kappa}_c$, shown with the red dashed line. For all plots, error bars are standard errors of the mean determined from the complex Langevin data.

The phase transition between a finite-temperature stripe and zFM phase is classified as first order and shown in Figure (2). The zFM is a spatially homogeneous, superfluid phase with ferromagnetic \hat{z} pseudospin order, so the $\mathbf{k} = \mathbf{0}$ momentum state occupation fraction and integrated \hat{z} magnetization M_z serve as good order parameters to show the presence of homogeneous superfluidity and \hat{z} magnetic order, respectively. In contrast, the vertically oriented stripe superfluid has two macroscopically occupied modes at non-zero $\mathbf{k} = (\pm\tilde{\kappa}, 0)$ and no net \hat{z} ferromagnetism. Figure (2a) shows discontinuities in each order parameter near $\tilde{\kappa} = 0.17$ for the zFM phase and signals the closure of the zFM-stripe metastability window. The stripe structures remain stable down to low spin-orbit coupling (SOC) strengths and may require prohibitively large simulation cells to observe stripe structure instabilities as $\tilde{\kappa} \rightarrow 0$.

For this first-order transition, we utilize the grand potential Ω to locate the precise boundary between the stripe and zFM phase at the prescribed temperature \tilde{T} and chemical potential μ . The phase with the lower grand potential is identified as the stable equilibrium phase in the phase diagram, so the SOC strength at the phase boundary $\tilde{\kappa}_c$ is determined by finding where the grand potential difference between the competing phases crosses zero. A representative phase boundary calculation is shown in Figure (2b) for $\tilde{T} = 0.5$ as an example. The crossing point was determined by linear interpolation, where the propagated error and covariance of the fitted slope and intercept provided an estimation of error for $\tilde{\kappa}_c$. For the example shown in Figure (2) at $\tilde{T} = 0.5$, the phase boundary point was determined to be $\tilde{\kappa}_c = 0.0914 \pm 0.006$, where a kink in Ω is observed (Figure (2c)).

Stripe to Emulsion Transition: Kosterlitz–Thouless Finite-Size Analysis

Near the critical temperature of the stripe to microemulsion transition, significant finite-size effects occur in estimates of the superfluid density ρ_{SF} , which obscure the value of the critical temperature. In 2D superfluid systems, a Kosterlitz–Thouless (KT) transition is expected and is characterized by a universal jump in the superfluid density (stiffness) [3] from a value of $\rho_{\text{SF}}(\tilde{T}_{\text{KT}}) = \frac{1}{\pi}\tilde{T}_{\text{KT}}$ to zero as the temperature is increased across \tilde{T}_{KT} , expressed using the dimensionless quantities employed in this study. However, the stripe to emulsion transition is broadened by the finite size of the simulation, which cannot capture the diverging correlation length and show a true jump in ρ_{SF} . As the system size increases, the decline of the superfluid stiffness sharpens in character to align with a universal jump.

In the stripe to microemulsion transition, the superfluid stiffness component that is perpendicular to the stripes' orientation ρ_{SF}^{xx} was used as the representative order parameter to perform finite-size scaling analysis. Although the superfluid stiffness parallel to the stripes ρ_{SF}^{yy} shows a similar decline, the normal component ρ_{SF}^{xx} experiences a full variation between 0 and 1 and serves as a more appropriate measure of the helicity or superfluidity modulus to align with the universal jump quantitatively. Data are plotted for $\tilde{\kappa} = 0.5$ in Figure (3a), where the decline in the superfluid density is steeper as the number of stripe periods increases.

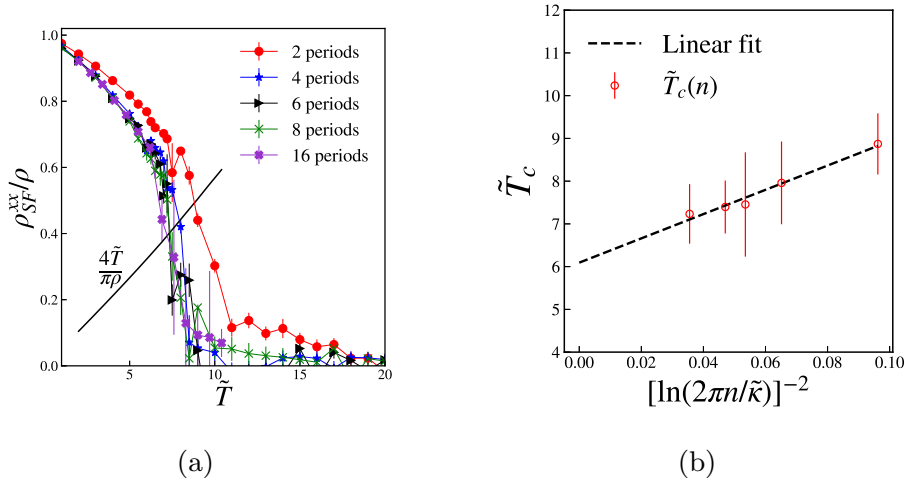


Fig. 3: Kosterlitz–Thouless-like transition at $\tilde{\kappa} = 0.5$, $\eta_g = 1.1$, and $\tilde{g} = 0.05$.
a. Superfluid fraction normal component $\rho_{\text{SF}}^{xx}/\rho$ plotted for several system sizes, denoted as the number of stripe periods n in the legend. Error bars are standard errors of the mean, determined from the Langevin-time averaging process. The nematic superfluid universal jump result is shown in the solid black curve. **b.** \tilde{T}_c scaling with system size using the scaling form in Equation (7), with a linear fit shown in the black dashed line. Error bars for each $\tilde{T}_c(n)$ were estimated from the slope and intercept covariance of an interpolated crossing between the $\rho_{\text{SF}}^{xx}(n)/\rho$ curve and the modified universal jump.

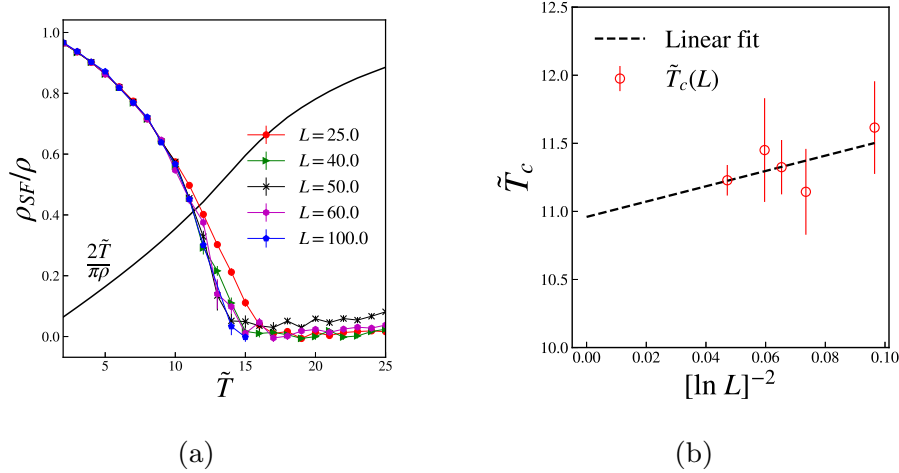


Fig. 4: Kosterlitz–Thouless transition at $\tilde{\kappa} = 0.0$, $\eta_g = 1.1$, and $\tilde{g} = 0.05$.
a. Superfluid fraction ρ_{SF}/ρ of the zFM phase plotted for several system sizes with length L . Error bars are standard errors of the mean, determined from the Langevin-time averaging process. The modified universal result for pseudospin-1/2 Bose gases is shown in the solid black curve. **b.** Scaling of the critical temperature with system size. Open red circles are determined from the crossing of the solid black curve $\rho_{\text{SF}}(\tilde{T}_{\text{KT}}) = \frac{2}{\pi}\tilde{T}_{\text{KT}}$ with superfluid density data at each system size. Points are plotted using the scaling form in Equation (7), with a linear fit shown in the black dashed line. Error bars for each $\tilde{T}_c(L)$ estimate were estimated from the slope and intercept covariance of an interpolated crossing between the $\rho_{\text{SF}}(L)/\rho$ curve and the modified universal jump.

For multi-species interacting Bose-Einstein condensates, the jump in the superfluid density is reported to deviate from the universal value [4–6], so careful consideration must be made in our finite-size analysis. For example, reference [4] showed that pseudospin-1/2 bosons without spin-orbit coupling ($\tilde{\kappa} = 0$) are expected to experience a jump at twice the universal result: $\rho_{\text{SF}}(\tilde{T}_{\text{KT}}) = \frac{2}{\pi}\tilde{T}_{\text{KT}}$. We follow reference [7], which estimated the modified universal jump as $\rho_{\text{SF}}(\tilde{T}_{\text{KT}}) = \frac{4}{\pi}\tilde{T}_{\text{KT}}$ for the stripe phase with isotropic SOC, which is a nematic superfluid in the thermodynamic limit. Furthermore, reference [6] showed that a nematic superfluid phase in $S = 1$ spinor condensates are best described by a KT transition with a similarly modified universal jump $\rho_{\text{SF}}(\tilde{T}_{\text{KT}}) = \frac{4}{\pi}\tilde{T}_{\text{KT}}$. The precise nature of the bound topological defects dictates the adjustment to the precise temperature at which the universal jump occurs. As such, a detailed analysis of the interplay among simultaneous superfluid phase, XY spin, and \hat{z} spin defects is left to a future study.

Following procedures outlined in references [4, 5, 8], we estimate a corrected Kosterlitz–Thouless critical temperature T_{KT} for systems with SOC ($\tilde{\kappa} > 0$) using the modified universal result. We extrapolate from the approximate critical temperatures at different system sizes, obtained from the crossing between the modified universal form $\rho_{\text{SF}}(\tilde{T}_{\text{KT}}) = \frac{4}{\pi}\tilde{T}_{\text{KT}}$ and the \hat{x} superfluid stiffness curves shown in Figure (3a). The crossing temperature at each system size was determined using linear interpolation. For systems without SOC ($\tilde{\kappa} = 0$),

the other modified universal result $\rho_{\text{SF}}(\tilde{T}_{\text{KT}}) = \frac{2}{\pi}\tilde{T}_{\text{KT}}$ for pseudospin-1/2 Bose gases was employed to produce the results shown in Figure (4), corresponding to the unbinding of half-vortex defects.

In a KT transition, finite-size corrections to the precise critical temperature are assumed to scale logarithmically in the following form:

$$\tilde{T}_c(L) = \tilde{T}_{\text{KT}} + \frac{b}{[\ln(L)]^2} \quad (7)$$

where L is the linear system size (simulation cell box length) and b is an arbitrary, non-universal parameter. The system size replaces the growing bulk correlation length near the critical transition. We assume such a logarithmic form for our finite-size analysis. Figures (3b) and (4b) shows a least squares linear fit of the $\tilde{T}_c(L)$ data as a function of inverse system size as described in equation (7). The intercept of the linear fit provides an estimate of the true Kosterlitz-Thouless transition temperature that corrects for finite-size errors. In the examples shown above, we estimate $\tilde{T}_{\text{KT}} = 6.13 \pm 0.96$ and $\tilde{T}_{\text{KT}} = 10.96 \pm 0.36$ for $\tilde{\kappa} = 0.5$ and $\tilde{\kappa} = 0$, respectively. \tilde{T}_{KT} error estimates are determined via the intercept's covariance from the linear fit to equation (7).

Microemulsion to Homogeneous Fluid Continuous Crossover

The transition between the structured normal fluid with microemulsion character and homogeneous normal fluid is best characterized as a continuous crossover. To quantify the crossover temperature, we monitored two features of the data: 1) The 2D isothermal compressibility $\kappa_T = -\frac{1}{A} \frac{dA}{dP}|_T$, and 2) a homogeneous order parameter, calculated as the fraction of $\mathbf{k} = \mathbf{0}$ mode occupation relative to the maximally occupied momentum state $\frac{N(\mathbf{k}=\mathbf{0})}{\max_{\mathbf{k}} N(\mathbf{k})}$ in the distribution. This order parameter is unity in a spatially homogeneous phase regardless of its normal or superfluid properties and trends to zero deep in the microemulsion where the $\mathbf{k} \neq \mathbf{0}$ ring modes are predominantly populated.

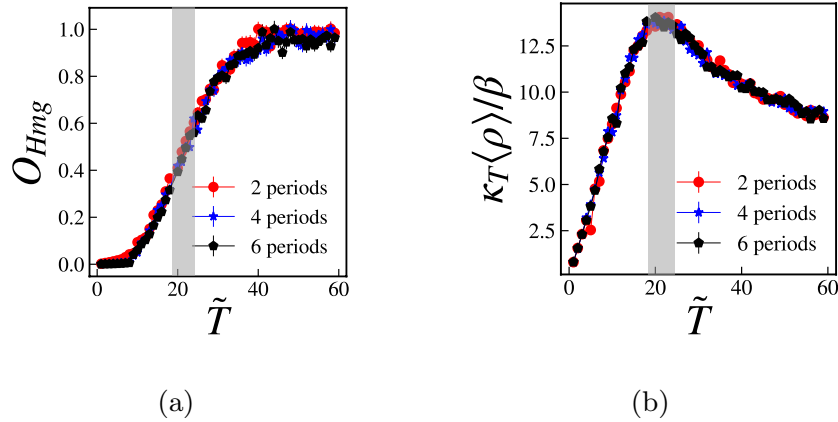


Fig. 5: Continuous crossover at $\tilde{\kappa} = 0.6$, $\eta_g = 1.1$, and $\tilde{g} = 0.05$. **a.** Homogeneous order parameter throughout the melting process. Error bars are standard errors of the mean. **b.** Isothermal compressibility, rescaled for better curve collapse. In both plots, error bars are standard errors of the mean.

Figure (5) presents data for $\tilde{\kappa} = 0.6$, showing the continuous crossover from the microemulsion to homogeneous fluid. As temperature increases after the stripe phase melts, the homogeneous order parameter increases monotonically (Figure (5a)) and saturates once the fluid is completely homogeneous. We fit the homogeneous order parameter data to a sigmoid and extract the crossover temperature $\tilde{T}_{\text{crossover}}$ as the approximate centroid of the temperature data with an estimated error derived from the covariance of the sigmoid's centroid. For this example, we determine the crossover temperature to be $\tilde{T}_{\text{crossover}} = 21.1 \pm 0.1$. This $\tilde{T}_{\text{crossover}}$ value showed excellent agreement with the approximate position of the peak in the compressibility at all system sizes, shown in Figure (5b). In both data sets, no statistically significant finite-size variations are observed.

References

- [1] Fredrickson, G. H. & Delaney, K. T. Direct free energy evaluation of classical and quantum many-body systems via field-theoretic simulation. *Proceedings of the National Academy of Sciences* **119** (18), e2201804119 (2022). URL <https://www.pnas.org/doi/full/10.1073/pnas.2201804119>. <https://doi.org/10.1073/pnas.2201804119>, publisher: Proceedings of the National Academy of Sciences .
- [2] Fetter, A. L. & Walecka, J. D. *Quantum Theory of Many-Particle Systems* (Courier Corporation, 2012). Google-Books-ID: t5_DAgAAQBAJ.
- [3] Nelson, D. R. & Kosterlitz, J. M. Universal Jump in the Superfluid Density of Two-Dimensional Superfluids. *Physical Review Letters* **39** (19), 1201–1205 (1977). URL <https://link.aps.org/doi/10.1103/PhysRevLett.39.1201>. <https://doi.org/10.1103/PhysRevLett.39.1201>, publisher: American Physical Society .
- [4] Kobayashi, M., Eto, M. & Nitta, M. Berezinskii-Kosterlitz-Thouless Transition of Two-Component Bose Mixtures with Intercomponent Josephson Coupling. *Physical Review Letters* **123** (7), 075303 (2019). URL <https://link.aps.org/doi/10.1103/PhysRevLett.123.075303>. <https://doi.org/10.1103/PhysRevLett.123.075303> .
- [5] Hickey, C. & Paramekanti, A. Thermal Phase Transitions of Strongly Correlated Bosons with Spin-Orbit Coupling. *Physical Review Letters* **113** (26), 265302 (2014). URL <https://link.aps.org/doi/10.1103/PhysRevLett.113.265302>. <https://doi.org/10.1103/PhysRevLett.113.265302> .
- [6] Mukerjee, S., Xu, C. & Moore, J. E. Topological Defects and the Superfluid Transition of the $s=1$ Spinor Condensate in Two Dimensions. *Physical Review Letters* **97** (12), 120406 (2006). URL <https://link.aps.org/doi/10.1103/PhysRevLett.97.120406>. <https://doi.org/10.1103/PhysRevLett.97.120406>, publisher: American Physical Society .
- [7] Jian, C.-M. & Zhai, H. Paired superfluidity and fractionalized vortices in systems of spin-orbit coupled bosons. *Physical Review B* **84** (6), 060508 (2011). URL <https://link.aps.org/doi/10.1103/PhysRevB.84.060508>. <https://doi.org/10.1103/PhysRevB.84.060508>, publisher: American Physical Society .
- [8] Radić, J., Natu, S. S. & Galitski, V. Stoner Ferromagnetism in a Thermal Pseudospin- 1 / 2 Bose Gas. *Physical Review Letters* **113** (18), 185302 (2014). URL <https://link.aps.org/doi/10.1103/PhysRevLett.113.185302>. <https://doi.org/10.1103/PhysRevLett.113.185302> .